# Qubit-photon interactions in a cavity: Measurement-induced dephasing and number splitting

Jay Gambetta,[1] Alexandre Blais,[1,2] D. I. Schuster,[1] A. Wallraff,[1,3] L. Frunzio,[1] J. Majer,[1] M. H. Devoret,[1] S. M. Girvin,[1] and R. J. Schoelkopf[1]

[1]*Department of Applied Physics and Department of Physics, Yale University, New Haven, Connecticut 06520, USA*

[2]*Département de Physique et Regroupement Québécois sur les Matériaux de Pointe, Université de Sherbrooke, Sherbrooke, Québec, Canada, J1K 2R1*

[3]*Department of Physics, ETH Zurich, CH-8093 Zürich, Switzerland*

(Received 13 February 2006; published 17 October 2006)

We theoretically study measurement-induced dephasing of a superconducting qubit in the circuit QED architecture and compare the results to those obtained experimentally by Schuster *et al.* [Phys. Rev. Lett. **94**, 123602 (2005)]. Strong coupling of the qubit to the resonator leads to a significant ac Stark shift of the qubit transition frequency. As a result, quantum fluctuations in the photon number populating the resonator cause dephasing of the qubit. We find good agreement between the predicted line shape of the qubit spectrum and the experimental results. Furthermore, in the strongly dispersive limit, where the Stark shift per photon is large compared to the cavity decay rate and the qubit linewidth, we predict that the qubit spectrum will be split into multiple peaks, with each peak corresponding to a different number of photons in the cavity.

DOI: 10.1103/PhysRevA.74.042318 PACS number(s): 03.67.Lx, 73.23.Hk, 74.50.+r, 32.80.−t

## I. INTRODUCTION

Superconducting qubits are promising building blocks for the realization of a quantum computer [1]. Several experiments have shown coherent control of a single qubit [2–6] and two-qubit experiments have been realized [7–11]. Recently, it was suggested that superconducting qubits can be strongly coupled to distributed or discrete *LC* circuits in a way that opens the possibility of studying quantum-optics-related phenomena in solid-state devices [12–16]. This concept has been successfully demonstrated experimentally [2,17–20] and effects associated with the quantum nature of the microwave electromagnetic field have now been seen in the form of vacuum Rabi splitting [17] and measurement-induced dephasing via photon shot noise [19]. In this paper we present a detailed analysis of the quantum fluctuations of the photon number in the cavity and its effect on the qubit spectrum. We also show that access to the extreme limit of strongly dispersive coupling should allow direct observation of the photon number distribution in the cavity.

An advantage of some of these circuit QED analogs of cavity QED is that the cavity presents a well-defined electromagnetic environment to the qubit which can lead to enhanced coherence times of the qubit [13]. This well-defined environment makes quantitative predictions for superconducting qubits more tractable. This was shown in Ref. [2] where we studied Rabi oscillations in a superconducting qubit strongly coupled to a superconducting transmission line resonator. Due to the detailed understanding of the measurement process, we were able to make quantitative predictions about the measured populations in the Rabi oscillations and observe high-visibility fringes [2]. Moreover, as we showed in Ref. [19], populating the strongly coupled resonator with a coherent microwave field can lead to a significant ac Stark shift of the qubit, even in the situation where detuning between the cavity and qubit frequencies is large. Due to the shot noise in the number of photons populating the resonator, this ac Stark shift leads to measurement-induced dephasing of the qubit. This is similar in spirit to the experiment on Rydberg atoms in a three-dimensional (3D) cavity reported in Refs. [21–24]. In those time-domain experiments, the visibility of Ramsey fringes was shown to decay with an increase of the strength of dispersive coupling to the cavity.

In this paper, we will expand on the theoretical model presented in our experimental paper [19] (hereafter referred to as the Letter) where we observed the ac Stark shift and measurement-induced dephasing in a circuit QED device. We will start in Sec. II with a brief review of the important features of circuit QED. In Sec. III the experimental results reported in the Letter will be reviewed. We then present in Sec. V two theoretical models describing measurement-induced dephasing. We first start with a simple model which assumes Gaussian fluctuations of the qubit's phase. This is the model that was briefly presented in the Letter to explain the experimental results. We then present a more general approach based on the positive-*P* representation [25] which does not require the Gaussian assumption. For the experimental parameters reported in the Letter, these two approaches give identical results. However, in the limit of strong coupling and very high-*Q* resonators, the second approach shows that qubit spectrum will exhibit structure at several distinct frequencies due to the underlying discrete energy levels of the cavity. That is, we predict that the qubit spectrum will split into multiple peaks, with each peak corresponding to a different number of photons in the cavity. We will refer to this as *number splitting* of the qubit spectrum. Experimental observation of this effect would be a direct demonstration of number quantization in the dispersive regime. We also discuss how, by using irradiation which is off resonant from both the cavity and the qubit, one can obtain substantial ac Stark shifts without significant dephasing and how this could be used as the basis of a phase gate for quantum computation.

 

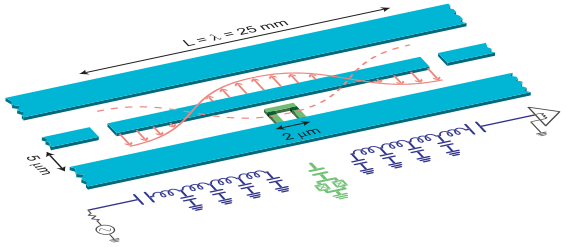


FIG. 1. (Color online) Schematic layout and lumped element version of the circuit QED implementation. A superconducting charge qubit (green) is fabricated inside a superconducting 1D transmission line resonator (blue).

## II. CAVITY QED WITH SUPERCONDUCTING CIRCUITS

### A. Jaynes-Cummings interaction

In this section, we briefly review the circuit QED architecture first introduced in Ref. [13] and experimentally studied in Refs. [2,17,19]. As shown in Fig. 1, the system consists of a superconducting charge qubit [1,12,26] strongly coupled to a transmission line resonator [27]. Near its resonance frequency $\omega_r$, the transmission line resonator can be modeled as a simple harmonic oscillator composed of the parallel combination of an inductor $L$ and a capacitor $C$. Introducing the annihilation (creation) operator $\hat{a}^{(\dagger)}$, the resonator can be described by the Hamiltonian

$$H_r = \hbar\omega_r \hat{a}^\dagger \hat{a}, \tag{2.1}$$

with $\omega_r = 1/\sqrt{LC}$. Using this simple model, one finds that the voltage across the $LC$ circuit (or, equivalently, on the center conductor of the resonator) is $V_{LC} = V^0_{\rm rms}(\hat{a}^\dagger + \hat{a})$, where $V^0_{\rm rms} = \sqrt{\hbar\omega_r/2C}$ is the rms value of the voltage in the ground state. An important advantage of this architecture is the extremely small separation $b \sim 5$ $\mu$m between the center conductor of the resonator and its ground planes. This leads to a large rms value of the electric field $E^0_{\rm rms} = V^0_{\rm rms}/b \sim 0.2$ V/m for typical realizations [2,17,19]. As illustrated in Fig. 1, by placing the qubit at an antinode of the voltage, it will strongly interact with the resonator through the large electric field $E^0_{\rm rms}$.

In the two-state approximation, the Hamiltonian of the qubit takes the form

$$H_q = -\frac{E_{\rm el}}{2}\hat{\sigma}_x - \frac{E_{\rm J}}{2}\hat{\sigma}_z, \tag{2.2}$$

where $E_{\rm el} = 4E_C(1-2n_g)$ is the electrostatic energy and $E_{\rm J} = E_{\rm J,max}\cos(\pi\Phi/\Phi_0)$ the Josephson energy. Here, $E_C = e^2/2C_\Sigma$ is the charging energy with $C_\Sigma$ the total box capacitance and $n_g = C_g V_g/2e$ the dimensionless gate charge with $C_g$ the gate capacitance and $V_g$ the gate voltage. $E_{\rm J,max}$ is the maximum Josephson energy and $\Phi$ the externally applied flux, with $\Phi_0$ the flux quantum.

Due to capacitive coupling with the center conductor, the gate voltage $V_g = V_g^{\rm dc} + V_{LC}$ has a dc contribution $V_g^{\rm dc}$ (coming from a dc bias applied to the input port of the resonator) and a quantum part $V_{LC}$. When working at the charge degeneracy point $n_g^{\rm dc} = 1/2$ where dephasing is minimized [4] and neglecting fast-oscillating terms, the resonator plus qubit Hamiltonian takes the Jaynes-Cummings form [13]

$$H_{\rm JC} = \hbar\omega_r \hat{a}^\dagger \hat{a} + \frac{\hbar\omega_a}{2}\hat{\sigma}_z - \hbar g(\hat{a}^\dagger \hat{\sigma}_- + \hat{\sigma}_+ \hat{a}), \tag{2.3}$$

where $\omega_a = E_{\rm J}/\hbar$ is the qubit transition frequency and $g = e(C_g/C_\Sigma)V^0_{\rm rms}/\hbar$ is the coupling strength.

As shown in Ref. [13], the qubit can be measured and coherently controlled by applying microwaves, of frequency $\omega_{\rm rf}$ and $\omega_{\rm s}$, respectively, to the input port of the resonator. This can be described by the additional Hamiltonian

$$H_{\rm D} = \sum_{j={\rm s,rf}} \hbar\varepsilon_j(t)(\hat{a}^\dagger e^{-i\omega_j t} + \hat{a}e^{+i\omega_j t}), \tag{2.4}$$

where $\varepsilon_j(t)$ is the amplitude of the external drives at rf and spectroscopy frequencies.

### B. Dispersive regime

In the situation where the qubit is strongly detuned from the cavity, $|\Delta| = |\omega_r - \omega_a| \gg g$, the total Hamiltonian $H_{\rm JC} + H_{\rm D}$ can be approximately diagonalized to second order in $g/\Delta$ to yield the following quantized version of the dynamical Stark shift Hamiltonian [13]

$$\begin{aligned} H_{\rm eff} = {} & \hbar\omega_r \hat{a}^\dagger \hat{a} + \frac{\hbar}{2}(\tilde{\omega}_a + 2\chi\hat{a}^\dagger\hat{a})\hat{\sigma}_z \\ & + \sum_{j={\rm s,rf}} \hbar\varepsilon_j(t)(\hat{a}^\dagger e^{-i\omega_j t} + \hat{a}e^{+i\omega_j t}) \\ & + \sum_{j={\rm s,rf}} \frac{\hbar g\varepsilon_j(t)}{\Delta}(\hat{\sigma}_+ e^{-i\omega_j t} + \hat{\sigma}_- e^{+i\omega_j t}). \end{aligned} \tag{2.5}$$

Here $\tilde{\omega}_a = \omega_a + \chi$ is the Lamb-shifted qubit frequency and we have defined $\chi = g^2/\Delta$. The term proportional to $\hat{a}^\dagger\hat{a}\hat{\sigma}_z$ can be interpreted as a shift of the qubit transition frequency depending on the photon number in the resonator (ac Stark shift) or as a pull on the resonator frequency by the qubit. As will be shown later, quantum noise in the photon number $\hat{a}^\dagger\hat{a}$ leads to dephasing of the qubit.

Dephasing due to coupling to the cavity field was also studied using Rydberg atoms coupled to a 3D microwave cavity [21–23]. In this experiment, atoms were sent one at a time through the cavity and interacted for a finite time with the field. The state of the atoms was finally read out by ionization [28]. Visibility of the Ramsey fringes was measured as a function of the detuning from the cavity and hence as a function of $\chi$. Dephasing was shown to increase with the strength of dispersive coupling $\chi$ to the cavity [22]. In this paper, we will instead consider dephasing of the qubit due to the resonator field by looking at the qubit spectrum as measured by transmission of the cavity field.

We note that, in practice, $\omega_{\rm s}$ is chosen to be close to $\tilde{\omega}_a$ and the last term of Eq. (2.5) with $\omega_{\rm s}$ causes Rabi flopping of the qubit. Moreover, as further discussed below, we choose $\omega_{\rm rf} = \omega_r - \Delta_r$ to measure the state of the qubit, where $\Delta_r$ is the detuning of the measurement probe from the bare cavity frequency. In this situation, the last term of Eq. (2.5) with $\omega_{\rm rf}$ is largely detuned from the qubit and does not lead to qubit

transitions. As first noted in the original proposal by Brune *et al.* [29,30] this measurement Hamiltonian is therefore highly quantum nondemolition (QND) [31] with respect to measurement of the qubit state. Conversely, if the dispersive coupling term is dominant in the Hamiltonian, then QND measurement of photon number is also possible. Physical implementation of QND readout for superconducting qubits has been achieved in the microwave regime [2,17–19], but values of the coupling $\chi$ large enough to allow QND readout in the dispersive regime for the photon number have not yet been achieved in any system. However, remarkable experiments on Rydberg atoms have achieved photon number readout in a nondispersive (i.e., degenerate) regime [21,32].

### C. Damping

Coupling to additional uncontrolled bath degrees of freedom leads to energy relaxation and dephasing in the system. Integrating out these degrees of freedom leaves the qubit plus cavity system in a mixed state $\rho(t)$ whose evolution can be described by the master equation [31]

$$\dot{\rho} = \mathcal{L}\rho = -\frac{i}{\hbar}[H,\rho] + \kappa\mathcal{D}[\hat{a}]\rho + \gamma_1\mathcal{D}[\hat{\sigma}_-]\rho + \frac{\gamma_\varphi}{2}\mathcal{D}[\hat{\sigma}_z]\rho, \tag{2.6}$$

where $\mathcal{D}[\hat{L}]\rho = (2\hat{L}\rho\hat{L}^\dagger - \hat{L}^\dagger\hat{L}\rho - \rho\hat{L}^\dagger\hat{L})/2$ describes the effect of the baths on the system in the Markov approximation. The last three terms of Eq. (2.6) correspond to loss of photons at rate $\kappa$, energy relaxation in the qubit at rate $\gamma_1$, and pure dephasing of the qubit at rate $\gamma_\phi$.

In the dispersive regime, the operators describing energy relaxation and dephasing should be transformed in the same way as was done in Eq. (2.5). This leads to small corrections, of order $(g/\Delta)^2$, to the master equation that are omitted here.

## III. EXPERIMENTAL RESULTS

In this section, we briefly review some of the experimental results already presented in the Letter. Only the results that are directly discussed in the present paper will be presented and the details of the experiment can be found in Refs. [2,17,19,27]. In the Letter, we reported spectroscopic measurements of the qubit as a function of measurement power. The qubit spectroscopic line is shown in Fig. 2 for two average photon numbers $\bar{n}$ in the resonator, corresponding to two input measurement powers. The relevant experimental parameters are $\Delta/2\pi = 105$ MHz, $g/2\pi = 5.8$ MHz, $\Delta_r/2\pi = 0$, and $\kappa/2\pi = 0.57$ MHz and a dephasing time (in the absence of power broadening) of $T_2 > 200$ ns. These values correspond to a relatively small cavity pull of $\chi/2\pi \approx 0.32$ MHz, or $\chi/\kappa \approx 0.56$ in units of the cavity linewidth. It is important to note that at these relatively low detunings $\Delta$, there can be a qubit contribution to the cavity linewidth.

As discussed in the Letter, at low measurement power, the line shape of the qubit spectrum is Lorentzian but as the measurement power increases, the line shape approaches a Gaussian. As shown in Fig. 3, this is also seen in the dependence of the half width at half maximum $\delta\nu_{\mathrm{HWHM}}$ of the qubit line shape on $\bar{n}$ which goes from $\propto\bar{n}$ to $\propto\sqrt{\bar{n}}$ as measurement power increases. This figure also shows theoretical results that will be discussed below.

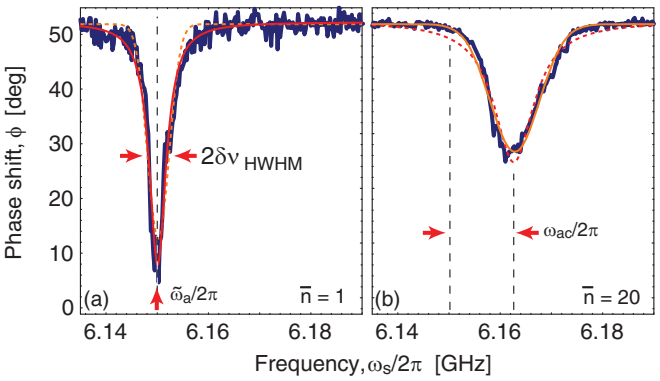


FIG. 2. (Color online) Measured spectroscopic lines (blue lines) at (a) intraresonator photon number $\bar{n} \approx 1$ with fit to Lorentzian line shape (solid line) and at (b) $\bar{n} \approx 40$ with fit to Gaussian line shape (solid line). Dashed lines are best fits to (a) Gaussian or (b) Lorentzian line shapes, respectively. The qubit transition frequency $\tilde{\omega}_a$ at low measurement power, the half width at half maximum $\delta\nu_{\mathrm{HWHM}}$, and the ac Stark shift $\omega_{\mathrm{ac}}$ of the lines are indicated.

In the Letter, we have already provided a theoretical explanation for this behavior. In Sec. V, we review and expand on this model. We then explain how in the limit of very large cavity pull, the results can be significantly different.

## IV. ac STARK SHIFT

In the lowest-order dispersive approximation [Eq. (2.5)] the predicted ac Stark shift $\omega_{\mathrm{ac}} = 2\chi\bar{n}$ will be a linear function of the mean photon number $\bar{n}$. However, this approximation

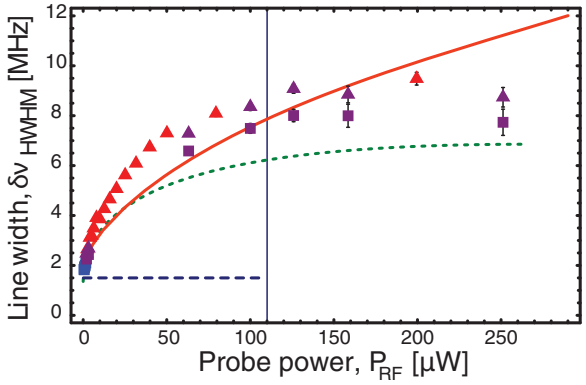


FIG. 3. (Color online) Full red curve: Measurement-broadened qubit linewidth $\delta\nu_{\mathrm{HWHM}}$ as a function of the input measurement power or average photon number as predicted by the lowest-order dispersive approximation. Green dotted curve: Same as red but taking into account the nonlinear reduction in the cavity pull and plotted as a function of input power. The symbols are the experimental results. Symbols and color scheme are described in the text. The vertical line indicates the critical photon number $n_{\mathrm{crit}}$. The parameters are those given in Sec. III. The blue dashed line is the calculated HWHM for $\Delta_r/2\pi = 32$ MHz. It clearly shows that measurement-induced dephasing is small at large $\Delta_r$ where information about the state of the qubit in the transmitted signal is also small. This can thus be used as the basis of a phase gate.

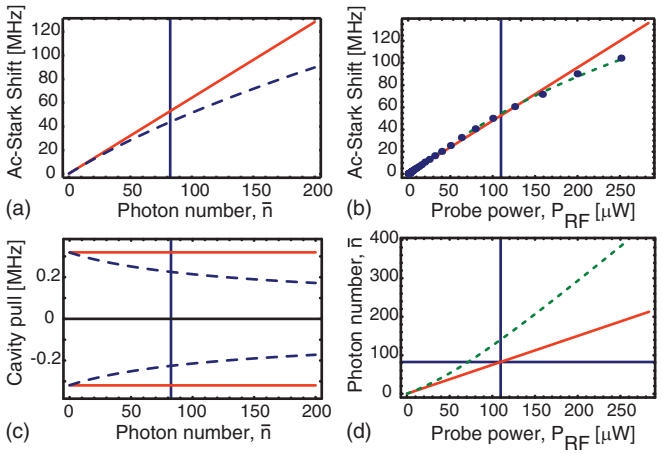


FIG. 4. (Color online) (a) Full red curve: ac Stark shift as a function of the average intracavity photon number using the lowest-order dispersive approximation. Dashed blue curve: ac Stark shift as a function of photon number calculated from the exact eigenvalues of the Jaynes-Cummings Hamiltonian. (b) Blue dots: experimentally measured ac Stark shift as a function of external microwave input power. Full red curve: Predicted ac Stark shift within the lowest-order dispersive approximation. The conversion factor from photon number to external microwave drive power was determined by fitting the red curve to the linear portion of the data at low power. Green dotted curve: Same as red but taking into account the nonlinear reduction in the cavity pull [see (c)] and the nonlinear increase in the average photon number [see (d)] with microwave drive power. For the particular experimental parameters these two effects almost cancel each other out and result in the green dotted line being nearly linear out to much greater input powers than expected. (c) Cavity pull as a function of average photon number $\bar{n}$. The red solid line is the result of the dispersive approximation ($\pm\chi$) while the dashed blue curve is obtained from the exact eigenvalues of the Jaynes-Cummings model. (d) Average photon number as a function of input power. The full red line is the result of the lowest-order dispersive dispersive approximation Eq. (4.1) fit to the data in (b) at low power. The dotted green line is the nonlinear model with $\chi$ replaced by $\chi(\bar{n})$ in Eq. (4.1) The vertical line in all plots indicates the critical photon number $n_{\mathrm{crit}}=\Delta^2/4g^2$, which indicates the scale at which the lowest order dispersive approximation breaks down. For the experimental parameters (given in Sec. III) $n_{\mathrm{crit}}\sim 82$ which corresponds (within the lowest-order dispersive approximation) to $P_{\mathrm{rf}}\sim 110\ \mu$W.

holds only at low photon numbers and breaks down on a scale given by the critical photon number $n_{\mathrm{crit}}=\Delta^2/4g^2$ [13]. This is illustrated in Fig. 4(a) where the ac Stark shift, calculated from the lowest-order dispersive approximation (red solid line) and the exact eigenvalues (blue dashed line) of the Jaynes-Cummings model [13] are plotted for the experimental parameters. Also shown in this figure is $n_{\mathrm{crit}}$ (vertical blue line) which for the experimental parameters is about 82 photons. Here we see that as $\bar{n}$ increases, the exact Stark shift begins to fall below the lowest-order dispersive approximation even before $\bar{n}$ reaches $n_{\mathrm{crit}}$.

In Fig. 4(b) the experimental results (solid blue points) are plotted as a function of probe power $P_{\mathrm{rf}}$ (extending up to powers larger than those presented in the Letter). To convert between $\bar{n}$ and $P_{\mathrm{rf}}$, we assume that $P_{\mathrm{rf}}=\lambda\hbar\omega_{\mathrm{rf}}p$ where $p$ is the photon flux at the resonator and $\lambda$ is a scaling factor that takes into account the large attenuation that is placed between the probe generator and the resonator (to eliminate blackbody radiation). From the lowest order dispersive approximation, the average photon number when driving the cavity at $\Delta_r=0$ is

$$\bar{n}=\frac{p\kappa/2}{(\kappa/2)^2+\chi^2}. \tag{4.1}$$

By using the lowest-order dispersive approximation for the ac Stark shift and the line of best fit to the experimental points (in the linear regime at low power) $\lambda$ can be determined. Doing this gives the red solid line in Figs. 4(b) and 4(d). The calibration shows that $n_{\mathrm{crit}}$ occurs at $\approx 110\ \mu$W. The experimental results clearly show the breakdown of the lowest-order dispersive approximation. The data points fall below the linear prediction but not nearly as much as the blue dashed curve in Fig. 4(a) predicts. In fact, the data points follow fairly closely the linear in $\bar{n}$ dependence of the lowest-order dispersive approximation in Eq. (2.5) for larger powers than expected (up to and well above $n_{\mathrm{crit}}$).

It is possible to understand why the experiment agrees with the simple dispersive approximation for larger probe powers than expected by considering the following simple model. We assume that, at these large powers, the ac Stark shift is still given by the dispersive approximation $2\chi\bar{n}$, but we now take into account the nonlinear cavity pull (which is $\chi$ at low $\bar{n}$). From the eigenvalues of the Jaynes-Cummings Hamiltonian the cavity pull can be calculated as a function of $\bar{n}$. This is shown in Fig. 4(c). From this figure, we see that the cavity pull reduces as the number of photons in the resonator is increased. We thus replace $\chi$ by $\chi(\bar{n})$. The second aspect of our simple model is the nonlinear dependence of the average photon number $\bar{n}$ on input power $P$ due to the power dependence of the cavity frequency. To account for this we simply replace $\chi$ in Eq. (4.1) with $\chi(\bar{n})$ and $\bar{n}$ becomes a nonlinear function of input power. This nonlinear dependence of the photon number on the input power is illustrated in Fig. 4(d) as the green dotted line. This is a precursor to bistability in this system [31]. Using these two expressions, we have for our simple model of the nonlinear ac Stark shift $2\chi(P)\bar{n}(P)$. This expression is plotted in Fig. 4(b) (green dotted line) with a new scaling factor $\lambda'\approx 0.905\lambda$ calculated by the best fit for the experimental data (here we use the complete data set). This simple model produces a result that is linear for a larger range of powers and is closely consistent with the experimental results. It happens that for the particular experimental parameters, the two nonlinear effects almost cancel each other out and result in the green dotted line being more linear than expected.

We emphasize that in the Letter, only the low-power (below $n_{\mathrm{crit}}$) part of the ac Stark shift was studied and was fitted only with the linear dispersive model. Comparison with the results of the nonlinear model shown here in Fig. 4(d) shows that the calibration of the cavity photon number in terms of the drive power is low by approximately 50% at the highest power shown in Fig. 5 of the Letter. We also emphasize that our treatment here of the nonlinearities is only approximate.

## V. MEASUREMENT-INDUCED DEPHASING

By monitoring the transmission of the cavity using heterodyne detection, one has access to the average of the cavity field $\langle \hat{a}(t) \rangle$. As shown in Ref. [13], the phase $\phi(t) = \arg\{\langle \hat{a}(t) \rangle\}$ is directly related to the population of the qubit $\langle \hat{\sigma}_z(t) \rangle$. As a result, by recording the phase $\phi(t)$ as a function of the excitation frequency $\omega_s$, one has access to the absorption spectrum of the qubit [25]

$$S(\omega) = \frac{1}{2\pi} \int_{-\infty}^{\infty} dt\, e^{i\omega t} \langle \hat{\sigma}_-(t) \hat{\sigma}_+(0) \rangle_s, \tag{5.1}$$

where the subscript $s$ implies that the expectation value is taken in the steady state. The dephasing rate can be determined through the half width at half maximum of $S(\omega)$ [33].

Using the quantum regression formula [25], the correlation function $\langle \hat{\sigma}_-(t) \hat{\sigma}_+(0) \rangle_s$ can be evaluated as

$$\langle \hat{\sigma}_-(t) \hat{\sigma}_+(0) \rangle_s = \begin{cases} \mathrm{Tr}[\hat{\sigma}_- e^{\mathcal{L}t} \hat{\sigma}_+ \rho_s], & t > 0, \\ \mathrm{Tr}[\hat{\sigma}_+ e^{-\mathcal{L}t} \rho_s \hat{\sigma}_-], & t < 0, \end{cases} \tag{5.2}$$

where $\rho_s$ is the steady-state density matrix. This allows us to rewrite the spectrum as

$$S(\omega) = \frac{1}{\pi} \mathrm{Re} \left( \int_0^{\infty} dt\, e^{i\omega t} \langle \hat{\sigma}_-(t) \hat{\sigma}_+(0) \rangle_s \right). \tag{5.3}$$

We start by calculating this spectrum by assuming Gaussian statistics for the qubit's phase noise. This approximation is sufficient for the experimental parameters considered above but breaks down in the situation where the cavity pull is large, $\chi \gg \kappa$. Moreover, this simple approach has the advantage of presenting the essential physics in a transparent way. We then show how to go beyond the Gaussian approximation by using the positive-$P$-function approach [25].

### A. Gaussian approximation for the phase

As mentioned above, quantum fluctuations $\delta n$ in the photon number around its average value $\bar{n}$ will lead to accumulation of a random relative phase between the amplitudes of the two basis states of the qubit and hence to dephasing. We first consider the situation where the qubit is prepared in a superposition $|\psi(0)\rangle = (|g\rangle + |e\rangle)/\sqrt{2}$ of its basis states and that the cavity is populated by a coherent state with average photon number $\bar{n}$. As it evolves under the dispersive Hamiltonian Eq. (2.5), the qubit superposition picks up a relative phase factor

$$\varphi(t) = \tilde{\omega}_a t + 2\chi \int_0^t dt' n(t'), \tag{5.4}$$

where $\tilde{\omega}_a = \omega_a + \chi$ is the Lamb-shifted qubit transition frequency. It is convenient to express the second term as its mean value plus fluctuations about the mean,

$$\varphi(t) \equiv \bar{\varphi} + \delta\varphi(t) = \tilde{\omega}_a t + 2\chi \bar{n} t + 2\chi \int_0^t dt'\, \delta n(t'), \tag{5.5}$$

with $\bar{n}$ the average photon number in the cavity leading to the ac Stark shift (see Fig. 4) and $\delta n(t)$ the random excursions about this mean.

In a frame rotating at the Lamb- and ac-Stark-shifted qubit transition frequency, we obtain for the correlation function ($t > 0$)

$$\begin{aligned} \langle \hat{\sigma}_-(t) \hat{\sigma}_+(0) \rangle_s &= \mathrm{Tr}[\hat{\sigma}_- e^{\mathcal{L}t} \hat{\sigma}_+ \rho_s] \\ &= \mathrm{Tr}[\hat{\sigma}_- e^{\mathcal{L}t} (|e\rangle\langle g|)] = e^{-\gamma_2 t} \langle e^{-i\delta\varphi(t)} \rangle, \end{aligned} \tag{5.6}$$

where $\gamma_2 = \gamma_1/2 + \gamma_\varphi$. This is the off-diagonal component of the reduced qubit density matrix. Assuming Gaussian statistics for the phase $\delta\varphi(t)$, the cumulant expansion is exact and we obtain [34]

$$\begin{aligned} \langle \hat{\sigma}_-(t) \hat{\sigma}_+(0) \rangle_s &\approx e^{-\gamma_2 t} e^{-\langle \delta\varphi^2 \rangle/2} \\ &= e^{-\gamma_2 t} \exp\left( -2\chi^2 \int \int_0^t dt_1 dt_2 \langle \delta n(t_1) \delta n(t_2) \rangle \right). \end{aligned} \tag{5.7}$$

This expression involves the photon-photon time correlator which for a two-sided symmetrically damped driven cavity takes the form [13]

$$\langle \delta n(t_1) \delta n(t_2) \rangle = \bar{n} e^{-(\kappa/2)|t_1 - t_2|}, \tag{5.8}$$

leading to

$$\langle \hat{\sigma}_-(t) \hat{\sigma}_+(0) \rangle_s = e^{-\gamma_2 t} \exp\left\{ -4\bar{n}\theta_0^2 \left[ \frac{\kappa|t|}{2} - 1 + \exp\left( -\frac{\kappa|t|}{2} \right) \right] \right\}, \tag{5.9}$$

where $\theta_0 = \tan^{-1} 2\chi/\kappa \approx 2\chi/\kappa$ is the magnitude of the accumulated phase shift for the transmitted photons due to the coupling with the qubit in the small-pull approximation ($\chi \ll \kappa$) and at $\omega_{\mathrm{rf}} = \omega_r$.

We now consider two simple limits of the above result. First, in the situation where the mean cavity photon number $\bar{n}$ is small, fluctuations of the photon number will only weakly contribute to dephasing. In this situation phase decay occurs on a long time scale with respect to $1/\kappa$. In this limit, $\exp(-\kappa|t|/2) \approx 0$ and Eq. (5.9) reduces to

$$\langle \hat{\sigma}_-(t) \hat{\sigma}_+(0) \rangle_s \approx \exp[-(\gamma_2 + 2\bar{n}\kappa\theta_0^2)|t|]. \tag{5.10}$$

In this situation, the measurement-induced dephasing only adds to the intrinsic dephasing rate $\gamma_2$. This is because, in this long-time limit, the phase undergoes a random walk process leading to an exponential decay of the coherence. The Fourier transform of this expression leads to a Lorentzian spectrum with half width at half maximum $\gamma_2 + \tilde{\Gamma}_{\mathrm{m}}$, where $\tilde{\Gamma}_{\mathrm{m}} = 2\kappa\bar{n}\theta_0^2$ is the measurement-induced dephasing rate in the small-pull limit (see the next section).

On the other hand, in the large-$\bar{n}$ limit, phase decay can occur on a time scale much shorter than the cavity lifetime, $t \ll \kappa^{-1}$. Indeed, since $\bar{n}$ is large, a small fraction of $\bar{n}$ leaking out of the cavity in a time $t \ll \kappa^{-1}$ conveys enough informa-

tion to infer the state of the qubit and hence to dephase it completely [35]. In this situation, expanding $\exp(-\kappa|t|/2)$ in Eq. (5.9), we obtain

$$\langle \hat{\sigma}_-(t)\hat{\sigma}_+(0)\rangle_s \approx \exp(-\gamma_2|t| - 2\bar{n}\chi^2 t^2). \tag{5.11}$$

The large-$\bar{n}$ limit does not lead to an exponential decay and the spectrum will be a convolution of a Lorentzian and a Gaussian. This corresponds to inhomogeneous broadening of the qubit due to the Poisson statistics of the coherent state populating the cavity. In this situation, the half width at half maximum therefore scales as $\sqrt{\bar{n}}$.

Using the full expression Eq. (5.9) and moving back to the laboratory frame, we obtain for the spectrum of the qubit in the Gaussian approximation for the phase,

$$\tilde{S}(\omega) = \frac{1}{2\pi}\sum_j \frac{(-2\tilde{\Gamma}_m/\kappa)^j}{j!}\frac{\tilde{\Gamma}_j/2}{(\omega - \tilde{\omega}_a - 2\bar{n}\chi)^2 + (\tilde{\Gamma}_j/2)^2}, \tag{5.12}$$

where $\tilde{\Gamma}_j = 2(\gamma_2 + \tilde{\Gamma}_m) + j\kappa$. The spectroscopic line shape is given by a sum of Lorentzians, all centered on the ac-Stark-shifted qubit transition but of different widths and weights.

As expected from the above discussion, we see from Eq. (5.12) that if the measurement rate $\tilde{\Gamma}_m$ is much smaller than the cavity decay rate $\kappa/2$, then only a few terms in the sum contribute and the spectrum is Lorentzian. On the other hand, when the measurement rate is fast compared to the cavity damping, the spectrum will be a sum of many Lorentzians, resulting in a Gaussian profile. In this situation, dephasing occurs before the cavity has had time to significantly change its state, leading to inhomogeneous broadening as discussed above.

The expression Eq. (5.12) for the spectrum can be summed analytically but yields an unsightly result which is not reproduced here. To compare with the experimental results, we evaluate numerically the half width at half maximum from $S(\omega)$. The results are plotted as a function of probe power in Fig. 3 (full red line). The agreement with the experimental results (symbols) is good, especially given that there are no adjustable parameters apart from $\gamma_2$, which only sets the value of the dephasing at $\bar{n}=0$. In this figure we have included more experimental points, for higher powers, than presented in Fig. 5 of the Letter. The experimental points presented here are obtained by fitting a Lorentzian (blue squares) and a Gaussian (red triangles) to the experimentally measured spectroscopic line (see Fig. 2). We then keep the fit that has the smallest variance or both points if the variances are approximately the same (purple squares and triangles). The error bars are the standard errors on the half width at half maximum obtained from the fit. This approach to extracting the error bar is different from what was presented in Fig. 5 of the Letter. In that case, the error bars represented the systematic difference between the Lorentzian and Gaussian fits and the points were the average value. From Fig. 3 (this paper) we see that the first seven points fit best to a Lorentzian while the later points fit best to a Gaussian, except for the higher powers where the error in the fit is approximately the same. The predicted crossover from Lorentzian to Gaussian is clearly seen.

There are several potential sources of discrepancy between the experimental and the theoretical results. One of them is the breakdown of the lowest-order dispersive approximation. Using the same simple nonlinear model as in Sec. IV, we plot in Fig. 3 the half width at half maximum as a function of input power (green dashed line). The effect of this correction is to reduce the width of the spectroscopy peaks.

The breakdown of the dispersive approximation can be seen by the dispersive result (red full line) overestimating the width at high powers. However, while the simple nonlinear model used here does correctly show saturation of the width at high powers, it is not a full treatment of the Jaynes-Cummings Hamiltonian and should not be considered too seriously. A complete investigation of the behavior of the system at very large photon numbers will require numerical investigation which is beyond the scope of this paper.

A further possible source of discrepancy comes from the fact that a constant spectroscopy power was used. Since the effective coupling strength $\chi$ is not constant with probe power, the effect of the spectroscopy power on the qubit will change with measurement probe power. As a result, spectroscopic power broadening [19] will also depend on measurement probe power. This effect has been taken into account in the green dashed curve of Fig. 3 but only to the accuracy of our simple model. Finally, environmental noise due to two-level systems activated at large photon number could be an additional cause of discrepancy.

### B. Beyond the Gaussian approximation

To go beyond the Gaussian approximation made in the last section, we solve the master equation Eq. (2.6) using the positive-$P$-function method [31]. Following Ref. [36], we first write the qubit-cavity density matrix as

$$\rho = \hat{\rho}_{ee}|e\rangle\langle e| + \hat{\rho}_{gg}|g\rangle\langle g| + \hat{\rho}_{eg}|e\rangle\langle g| + \hat{\rho}_{ge}|g\rangle\langle e|, \tag{5.13}$$

where $\hat{\rho}_{ij}$ acts only in the cavity Hilbert space. As shown in Appendix A, this leads to four coupled differential equations for the operators $\hat{\rho}_{ij}$. In the absence of qubit mixing ($T_1$ processes), solving these coupled equations yields the time-evolved full density matrix

$$\begin{aligned}\rho(t) = {} & c_{ee}(0)|e\rangle\langle e| \otimes |\alpha_+(t)\rangle\langle\alpha_+(t)| \\ & + c_{gg}(0)|g\rangle\langle g| \otimes |\alpha_-(t)\rangle\langle\alpha_-(t)| + c_{eg}(t)|e\rangle\langle g| \otimes |\alpha_+(t)\rangle \\ & \times\langle\alpha_-(t)| + c_{ge}(t)|g\rangle\langle e| \otimes |\alpha_-(t)\rangle\langle\alpha_+(t)|,\end{aligned} \tag{5.14}$$

where

$$c_{eg}(t) = \frac{a_{eg}(t)}{\langle\alpha_-(t)|\alpha_+(t)\rangle} \tag{5.15}$$

describes the decay of the qubit phase coherence. In the above expression, we have

$$a_{eg}(t) = a_{eg}(0)\exp[-i(\tilde{\omega}_a - i\gamma_2)t] \times \exp\left(-i2\chi\int_0^t \alpha_+(t')\alpha_-^*(t')dt'\right) \quad (5.16)$$

and $a_{ge}(t)=a_{eg}^*(t)$ with

$$\alpha_+(t) = \alpha_+^s + \exp[-(\kappa/2 + i\chi + i\Delta_r)t][\alpha_+(0) - \alpha_+^s], \quad (5.17)$$

where $\alpha_+^s=-i\varepsilon_{\rm rf}/(\kappa/2+i\chi+i\Delta_r)$. Moreover, we have

$$\alpha_-(t) = \alpha_-^s + \exp[-(\kappa/2 - i\chi + i\Delta_r)t][\alpha_-(0) - \alpha_-^s], \quad (5.18)$$

with $\alpha_-^s=-i\varepsilon_{\rm rf}/(\kappa/2-i\chi+i\Delta_r)$. In these expressions, $\alpha_\pm^s$ represents the steady-state value of the field $\langle\hat{a}\rangle$ given that the qubit is in either its ground $(-)$ or excited $(+)$ state. Recall that $\Delta_r$ is the detuning of the measurement beam from the bare cavity frequency.

In the limit $\kappa t \gg 1$ discussed previously, the decay of $a_{eg}(t)$ is given by

$$a_{eg}(t) \sim a_{eg}(0)\exp[-(\gamma_2 + \Gamma_{\rm m})t], \quad (5.19)$$

where

$$\Gamma_{\rm m} = -2\chi\,{\rm Im}(\alpha_+^s\alpha_-^{s*}) = \frac{(\bar{n}_+ + \bar{n}_-)\kappa\chi^2}{\kappa^2/4 + \chi^2 + \Delta_r^2} \quad (5.20)$$

is the generalized measurement-induced dephasing rate. In this expression,

$$\bar{n}_\pm = |\alpha_\pm^s|^2 = \frac{\varepsilon_{\rm rf}^2}{\kappa^2/4 + (\Delta_r \pm \chi)^2} \quad (5.21)$$

is the stationary average number of photons in the cavity when the qubit is in the excited $(+)$ or ground $(-)$ state. At small pulls, as is the case for the experimental parameters quoted in Sec. III, the measurement-induced dephasing rate is largest at $\Delta_r=0$ (see Fig. 5, blue dashed line). At large pulls, cavity transmission decreases at $\Delta_r=0$ and, as illustrated in Fig. 5 (red solid line), the maximum dephasing rate then occurs at $\Delta_r=\pm\sqrt{\chi^2-\kappa^2/4}$. As we increase $\chi$, the information about the state of the qubit is conveyed more by the amplitude than the phase of the transmitted beam.

From the above, we see explicitly that by introducing a probe $(\varepsilon_{\rm rf})$ we cause the coherence terms $a_{eg}(t)$ to exponentially decay at a rate $\Gamma_m$ thereby leaving the system in a mixed state with perfect correlation between the eigenstates of $\hat{\sigma}_z$ and the pointer states $|\alpha_+\rangle$ and $|\alpha_-\rangle$. As a result, if the pointer states are well separated in phase space, we can regard the cavity as a meter which performs a von Neumann projective measurement of the qubit observable $\hat{\sigma}_z$.

A measure of the distinguishability of the cavity states is $D=|\alpha_+-\alpha_-|^2$ [31]. If this is large such that $|\langle\alpha_-|\alpha_+\rangle| = \exp(-D)$ is small, then the two pointer states are well separated and easily distinguishable. In the steady state, $D$ is given by

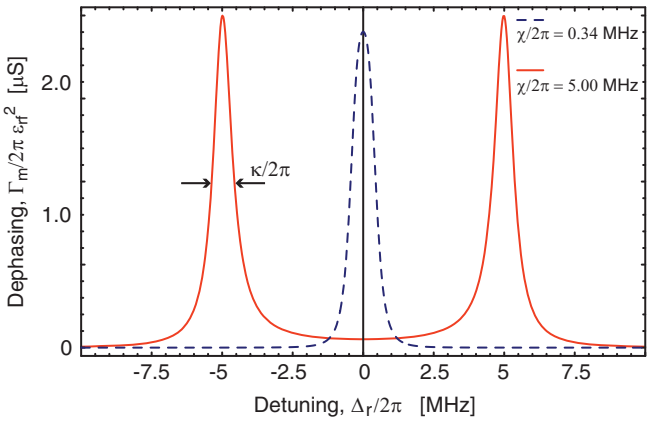


FIG. 5. (Color online) Measurement-induced dephasing rate $\Gamma_{\rm m}$ as a function of the detuning $\Delta_r$ between the bare resonator frequency $\omega_r$ and the measurement drive frequency $\omega_d$. The dephasing rate is divided by the measurement power $\varepsilon_{\rm rf}^2$ since it only changes the overall scale and not the structure of $\Gamma_{\rm m}$. The blue (dashed) line corresponds to the experimental parameters given in Sec. III. The red (full) line has the same parameters but a larger cavity pull $\chi/2\pi=5$ MHz.

$$D_{\rm s} = \frac{2(\bar{n}_+ + \bar{n}_-)\chi^2}{\kappa^2/4 + \chi^2 + \Delta_r^2}, \quad (5.22)$$

which is related to $\Gamma_{\rm m}$ in the following way:

$$\Gamma_{\rm m} = \frac{D_{\rm s}\kappa}{2}. \quad (5.23)$$

That is, as the measurement becomes more projective in the $\hat{\sigma}_z$ basis, the qubit dephases faster. This is a clear example of measurement induced dephasing and of the fundamental limit which exists between acquiring information about a quantum system and dephasing of that system [35]. Note that, as shown in Appendix B, $D_{\rm s}$ can also be related to the measurement time. The present system is a factor of 4 away from the quantum limit. One factor of 2 comes from the fact that we are using a symmetric resonator and only looking at the transmission. Half of the information is lost in the unmeasured reflected signal [13]. The other factor of 2 comes from the use of heterodyne rather than homodyne detection. As a result and as shown in Appendix B, the quantum limit can be reached by using asymmetric resonators and homodyne detection of the transmitted field.

#### *1. The qubit absorption spectrum*

To evaluate the qubit's spectrum, we first need to calculate the correlation function $\langle\hat{\sigma}_-(t)\hat{\sigma}_+(0)\rangle_s$. Note that (as discussed in Appendix A) in calculating this particular correlation function we do not need to assume that $T_1$ is infinite. This is because it depends only on the off-diagonal coherences and these are not mixed by a $T_1$ process. Using Eq. (5.2) and the above results, the correlator can be shown to be $(t>0)$

$$\langle \hat{\sigma}_-(t)\hat{\sigma}_+(0)\rangle_s = a_{eg}(t), \tag{5.24}$$

with the initial condition $\alpha_+(0)=\alpha_-(0)=\alpha_-^s$. Using Eq. (5.16) with the above initial condition yields

$$\langle \hat{\sigma}_-(t)\hat{\sigma}_+(0)\rangle_s = \exp[-(\gamma_2+\Gamma_m)t - i(\tilde{\omega}_a+B)t] \times \exp(-Ae^{-(\kappa/2+i\chi+i\Delta_r)t})\exp(A), \tag{5.25}$$

where

$$A = -i2\chi\frac{(\alpha_-^s-\alpha_+^s)\alpha_-^{s*}}{\kappa/2+i\chi+i\Delta_r} = D_s\frac{\kappa/2-i\chi-i\Delta_r}{\kappa/2+i\chi+i\Delta_r}, \tag{5.26}$$

$$B = 2\chi\,\mathrm{Re}(\alpha_+^s\alpha_-^{s*}) = \chi(\bar{n}_+ + \bar{n}_-) - \chi D_s. \tag{5.27}$$

From the above expression, we see that the time dependence of the correlation function is given by three terms. The first one involves $\Gamma_m$ and is simply the Lorentzian part of the measurement-induced dephasing spectrum we have seen before. The second is a frequency shift $B$ that contains a negative term $-\chi D_s$ which gives rise to negative frequency contributions in the spectrum. The last relevant term goes as $A\exp\{[\kappa/2+i(\chi+\Delta_r)]t\}$ and gives rise to non-Lorentzian spectra.

From the expression for the correlation function, it is simple to obtain the spectrum:

$$S(\omega) = \frac{1}{\pi}\sum_{j=0}^{\infty}\frac{1}{j!}\,\mathrm{Re}\left(\frac{(-A)^j e^A}{\Gamma_j/2 - i(\omega-\omega_j)}\right), \tag{5.28}$$

where $\Gamma_j=2(\gamma_2+\Gamma_m)+j\kappa$ and $\omega_j=\tilde{\omega}_a+B+j(\chi+\Delta_r)$. The spectrum, as in the Gaussian approximation, can be written as a sum over different photon numbers $j$. In the limit of $(\Delta_r+\chi)$ much different from $\kappa/2$, the spectrum is a sum of Lorentzians with decay rate $\Gamma_j/2$. However, unlike Eq. (5.12) where each Lorentzian is centered at the ac-Stark-shifted frequency, here each peak has its own frequency shift $\omega_j$. As a result, the full theory predicts that the spectrum need not be symmetric whereas in the Gaussian theory only symmetric spectra are possible. Furthermore, in the limit that $\chi$ is much larger than $\kappa$, $A\to D_s$ and the spectral weights become Poisson distributed with mean $D_s$. The peaks are separated by $(\chi+\Delta_r)$ and the first one is at the frequency $\tilde{\omega}_a+B$. That is, the average frequency, which is the ac Stark shift, occurs at

$$\omega_{\mathrm{ac}} = B + (\chi+\Delta_r)D_s = 2\chi n_-. \tag{5.29}$$

Taking this limit further with $\chi$ much larger than the widths $\Gamma_j$, the individual peaks will become distinguishable. This is discussed further below.

It is interesting to point out that in the limit of large $\bar{n}_-$ (or $\bar{n}_+$) the results obtained here and those obtained in the Gaussian approximation agree. This can be seen by expanding the exponent $A\exp\{[\kappa/2+i(\chi+\Delta_r)]t\}$ in Eq. (5.25) to order $t^2$:

$$\langle \hat{\sigma}_-(t)\hat{\sigma}_+(0)\rangle_s \approx \exp\left(-(\gamma_2+i\tilde{\omega}_a+i2\chi\bar{n}_-)t - \frac{D_s}{2}[\kappa^2/4+(\Delta_r+\chi)^2]|t|^2\right). \tag{5.30}$$

For $\Delta_r=0$, $\bar{n}_-=\bar{n}_+\equiv\bar{n}$ and we recover Eq. (5.11) in the laboratory frame. As a result, in the large-$\bar{n}$ limit, both the Gaussian approximation and the above theory converge to give the same Gaussian spectrum. It is only when $\bar{n}$ is small that the theories have different predictions. This will be discussed further in Sec. V B 3.

The half width at half maximum of the spectrum obtained from the full expression Eq. (5.28) is plotted at $\Delta_r=0$ as a function of $\bar{n}$ in Fig. 3 using the experimental parameters given in Sec. III. Since the experiment was done in the limit $\chi<\kappa/2$, the results obtained from Eq. (5.28) cannot be distinguished from those obtained from the Gaussian approximation Eq. (5.12). This is because in the small-cavity-pull limit $\Gamma_m\to\tilde{\Gamma}_m$ and therefore $A\to 2\tilde{\Gamma}_m/\kappa$, $B\to 2\bar{n}\chi$. That is, to see the breakdown of the Gaussian approximation at small $\bar{n}$ requires a larger cavity pull.

### 2. Phase gate

As discussed above and in Appendix B, measurement causes dephasing of the qubit. This is a clear illustration of the Heisenberg-type relation between rate of information gain and dephasing $\Gamma_m$ [35]. However, irradiation at the rf frequency does not have to induce dephasing of the qubit. Indeed, the qubit pulls the resonator frequency up or down causing a state-dependent phase shift for photons near the cavity frequency. But, in the low-$\chi$ limit, photons off resonant from the resonator have phase shifts nearly independent of the qubit state. These photons do not become entangled with the qubit, and hence do not cause dephasing.

This can be understood more quantitatively in Fig. 5, where it can be seen that the dephasing rate is significant only on a frequency range $\kappa$ around the pulled resonator frequency. In this figure, we have fixed the input power and scanned $\Delta_r$. In Fig. 6, we rather keep the number of photons in the cavity fixed ($\bar{n}_-=2$) and scan $\Delta_r$. We see that at large detunings, the dephasing rate scales as $\Delta_r^{-2}$. As a result, off-resonant irradiation can produce large ac Stark shifts ($\omega_{\mathrm{ac}}$) with minimal dephasing of the qubit. This can be used as a single-bit phase gate for quantum computation.

The observed asymmetry in the large-$\chi$ case (red solid line of Fig. 6) is a result of the fact $\Gamma_m$ depends on $\bar{n}_-$ and $\bar{n}_+$. By writing $\bar{n}_+$ as

$$\bar{n}_+ = \bar{n}_-\frac{\kappa^2/4+(\Delta_r-\chi)^2}{\kappa^2/4+(\Delta_r+\chi)^2}, \tag{5.31}$$

we see that at fixed $\bar{n}_-$, $\bar{n}_+$ can be large for negative $\Delta_r$. Thus the overall measurement induced dephasing will be large in that region.

The quality factor for this single-qubit gate, $Q$, can be defined as the coherent phase rotation that can be realized in the total dephasing time $(T_2^{-1}+\Gamma_m)^{-1}$ [4]. That is,

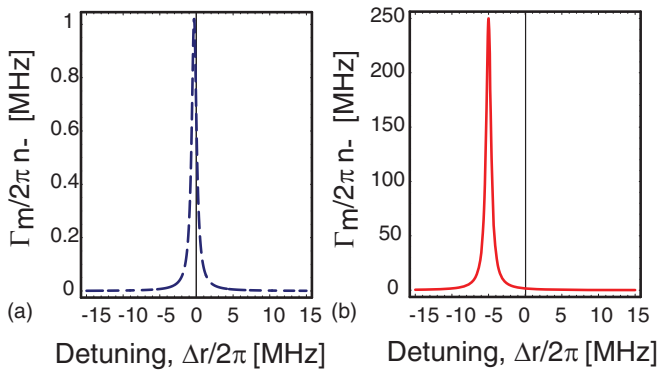


FIG. 6. (Color online) Dephasing rate $\Gamma_m$ as a function of the detuning $\Delta_r$ between the bare resonator frequency $\omega_r$ and the measurement drive frequency $\omega_d$ for fixed $\bar{n}_-=2$. (a) Experimental parameters given in Sec. III. (b) Same as (a) but with a larger cavity pull $\chi/2\pi=5$ MHz.

$$Q=\frac{\omega_{\mathrm{ac}}}{2(T_2^{-1}+\Gamma_m)}\approx\frac{(\Delta_r+\chi)^2}{2\kappa\chi} \tag{5.32}$$

in the large-pull limit and in the ideal situation where dephasing is limited by photon shot noise. Moreover, similarly to Rabi oscillations that have been demonstrated experimentally [2], this phase gate could be realized on a time scale which is much faster than $1/\kappa$ since for off-resonant irradiation, the cavity is only virtually populated.

To show that the dephasing is minimal during the phase gate, we have calculated using Eq. (5.28) the linewidth of the qubit spectrum as a function of input power for the experimental parameters and a large positive detuning $\Delta_r/2\pi=32$ MHz (well away from the peak shown in Fig. 6). This is shown in Fig. 3 as a blue dashed line. Here we see that in the dispersive model, there is no additional dephasing due to the off-resonant irradiation. That is, the predicted linewidth stays constant at $\gamma_2$ for the input powers plotted. At the critical photon number, $n_{\mathrm{crit}}=\Delta^2/4g^2$ the quality factor for the above experimental parameters is 17.3. This quality factor can, however, be easily increased by optimizing the system parameters [37]. For example at $g/2\pi=100$ MHz and $\Delta/2\pi=1000$ MHz a quality factor of 157 can be reached. (This value is entirely limited by the current value of $T_2\sim 500$ ns and not by the direct infidelity of the phase gate.) An advantage of this rf approach over a dc pulse of the flux or gate charge is that the logical operation can be realized while biased at the sweet spot.

### 3. Number splitting

As explained in the previous sections, the Gaussian model and the $P$-function approach agree in the small-pull limit $\chi \ll \kappa/2$. In the large-pull case, the predicted behavior is, however, substantially different. Indeed, when the Lorentzians in Eq. (5.28) are separated in frequency by more than their width, the spectrum $S(\omega)$ will be split into many peaks with each peak corresponding to a different photon number in the cavity. Number splitting was also predicted by Dykman and Krivoglaz for a different situation, namely, an undriven cavity coupled to a thermal bath [38]. The number splitting for our case (driven cavity at zero temperature) is illustrated in Figs. 7 and 8. In Fig. 7, the spectrum is shown as a function of frequency and of the detuning $\Delta_r$ for a fixed $\chi/\kappa=100$. In Fig. 7(a) ($\Delta_r>0$), $\bar{n}_-$ is fixed and equal to 2 whereas in Fig. 7(b) ($\Delta_r<0$), $\bar{n}_+=2$. The choice of fixing either $n_+$ or $n_-$ was made so that there is always a small number of photons in the cavity independent of the state of the qubit. For example, for $n_-$ fixed, the number of photons in the cavity when the qubit is excited, $n_+$, would be small for $\Delta_r>0$, equal to $n_-$ at $\Delta_r=0$, and very large at $\Delta_r=-\chi$. The inset shows a cross section at $\Delta_r/\kappa=100$ ($\Delta_r=\chi$). For this value of $\Delta_r/\kappa$, the peaks are very well separated and the integrated area under each peak obeys Poisson statistics. It is interesting to stress that only at $\Delta_r=\chi$ does the spectrum have a simple Poisson distribution corresponding to a coherent state with average photon number $\bar{n}_-=2$. At $\Delta_r<\chi$ there are more peaks than expected for a coherent state of this amplitude. Furthermore, at $\Delta_r=-\chi$ the spectrum is single peaked.

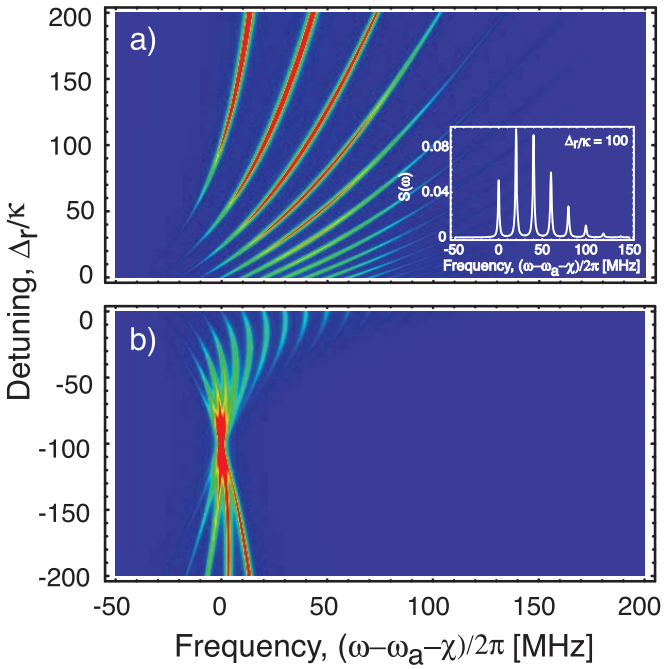


FIG. 7. (Color online) Spectrum $S(\omega)$ as a function of detuning $\Delta_r/\kappa$ at fixed cavity pull $\chi/\kappa=100$. The dephasing rate was set to the conservative value of $\gamma_2=7.6\kappa$. The average photon number in the cavity was fixed to $\bar{n}_-=2$ in (a) ($\Delta_r\geqslant 0$) and we choose $\bar{n}_+=2$ in (b) ($\Delta_r\leqslant 0$). This implies that the measurement beam power changes with detuning. Inset: Spectrum at $\Delta_r=\chi=100\kappa$. At this detuning, the peaks are split by $2\chi$. More generally, they are split by $\chi+\Delta$. Large detuning yields large splitting but, as shown in Fig. 5, this can be at the expense of a small measurable phase shift in the transmitted field.

In Fig. 8, the spectrum is shown as a function of the cavity pull $\chi/\kappa$ for a detuning of $\Delta_r=\chi$, such that the cavity is always driven at the pulled frequency $\omega_r-\chi$ corresponding to the qubit in the ground state. In these plots, we have taken $\gamma_2=7.6\kappa$. Assuming an experimentally realistic value of $\kappa/2\pi\sim 100$ kHz [27], this corresponds to a conservative $T_2=200$ ns [2]. As seen in Fig. 8, for these parameter values, the peaks should be resolvable experimentally starting

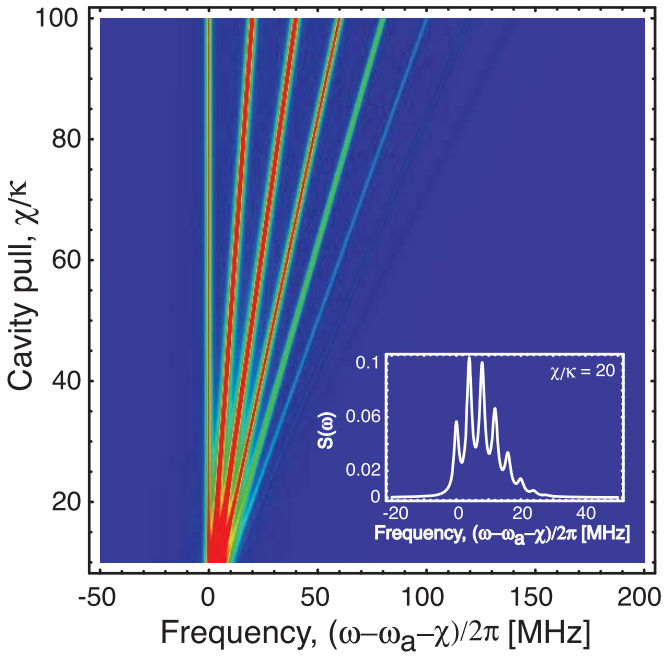


FIG. 8. (Color online) Spectrum $S(\omega)$ as a function of the cavity pull $\chi/\kappa$. The detuning is $\Delta_r=\chi$ such that the cavity is always driven at the dressed frequency $\omega_r-\chi$. Other parameter values are the same as in Fig. 7. Inset: Spectrum at $\chi/\kappa=20$. At this experimentally realistic value of the cavity pull, the number splitting should be resolvable.

around $\chi/\kappa\sim 20$ (inset in Fig. 8). Achieving $\chi/\kappa\sim 20$ in the dispersive limit ($g/\Delta\lesssim 0.1$) requires $g/2\pi\sim 20$ MHz. This value of $g$ was already realized experimentally [2] and therefore the experimental observation of number splitting seems feasible.

The behavior described above can be understood simply as ringing of a high-$Q$ resonator when its resonance frequency is suddenly changed when the qubit changes state. Equivalently we can think of this as a Raman process in which drive photons in the cavity at the time of the transition are lifted up to the final cavity frequency. As discussed previously, the calculation of the spectrum assumes that the qubit is initially in the ground state with the measurement beam turned on at a frequency $\omega_d$ detuned by $\Delta_r$ from the bare resonator frequency $\omega_r$. In the calculation of the correlation function $\langle\hat{\sigma}_-(t)\hat{\sigma}_+(0)\rangle_s$, the qubit is flipped to the excited state at time $t=0$ and the overlap with the ground state is calculated at time $t$. When the qubit is flipped, the dressed resonator frequency is suddenly changed from $\omega_r-\chi$ to $\omega_r+\chi$. Depending on the frequency of the measurement drive and the quality factor of the cavity, this sudden change will cause ringing in the cavity. This is illustrated in Fig. 9 where the distance $D(t)=|\alpha_+(t)-\alpha_-(t)|^2$ is plotted as a function of time for two values of $\chi/\kappa$. For the moderate value of $\chi/\kappa=5$ (red full line), the distance is seen to undergo large oscillations before settling to the steady-state value $D_s$. For the low $\chi/\kappa$ ratio of 0.1 (blue dashed line) there is no ringing due to the abrupt change of dressed cavity frequency, and the distance simply rises to $D_s$.

The ringing is also shown in the inset of Fig. 9 where the real and imaginary parts of the cavity field $\alpha_+(t)$ are plotted

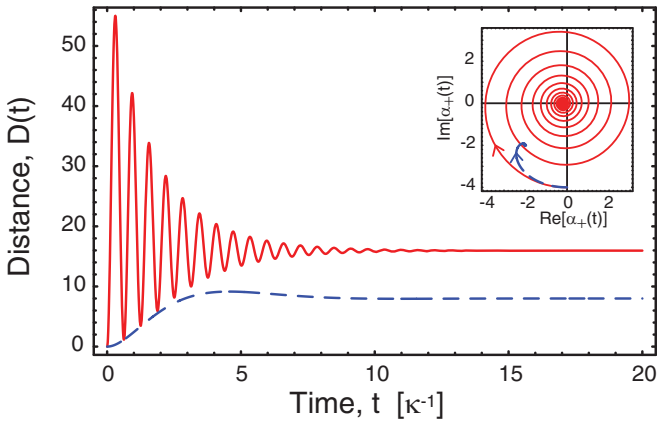


FIG. 9. (Color online) Distance $D(t)=|\alpha_+(t)-\alpha_-(t)|^2$ as a function of time for $\Delta_r=\chi$ and $\varepsilon_{\rm rf}=2\kappa$. The red (full) line corresponds to $\chi/\kappa=5$ and the blue (dashed) line to $\chi/\kappa=0.1$. Other parameter values are the same as in Fig. 7. Inset: Real and imaginary parts of the cavity field $\alpha_+(t)$ as a function of time. The arrows indicate direction of time.

as a function of time, again for $\chi/\kappa=0.1$ and 5. In the low-$Q$ case, as the qubit flips, the cavity field settles to its new steady-state value without large excursions in the field amplitude, and therefore large changes in photon number. Only a few different photon numbers contribute and the corresponding spectrum is single peaked as expected. In the high-$Q$ case, the field amplitudes performs many cycles before settling to the steady-state value. The cavity therefore probes a large range of photon numbers and the spectrum shows multiple peaks. In the time domain we can see that the qubit correlator, Eq. (5.25), has period recurrences provided $\chi\gg\kappa$. It is these recurrences in time which give peaks in the spectrum. These time domain recurrences were observed in the resonant regime ($\Delta=\Delta_r=0$) with Rydberg atoms in Ref. [24].

In the case where $\Delta_r=-\chi$ ($\omega_d=\omega_r+\chi$), the cavity is driven at the dressed cavity frequency corresponding to the qubit in the excited state. In this situation, flipping the qubit does not produce any inelastic Raman scattering (ringing) since the photons are already at the final cavity frequency. This is seen in Fig. 7 at $\Delta_r/\kappa=-100$ where the spectrum is single peaked.

Remarkably, when the detuning is such that $\Delta_r<\chi$, and as can be seen in Fig. 7, the spectrum has peaks at negative frequencies (i.e., below $\tilde{\omega}_a$) as well as more peaks than expected. In particular, in the limit that $\chi\gg\kappa$ and at $\Delta_r=0$, the frequencies start at $\tilde{\omega}_a-2\bar{n}_-\chi$ with peak separation $\chi$ and the spectral weights have a Poisson distribution with mean $4\bar{n}$ and not $\bar{n}$. To understand the presence of these peaks, we move the dispersive Hamiltonian Eq. (2.5) to the frame defined by the unitary operator

$$\hat{U}=\hat{\Pi}_+\hat{D}[\alpha_+]+\hat{\Pi}_-\hat{D}[\alpha_-]. \tag{5.33}$$

Here $\hat{D}[\alpha]$ is the displacement operator for the cavity defined by

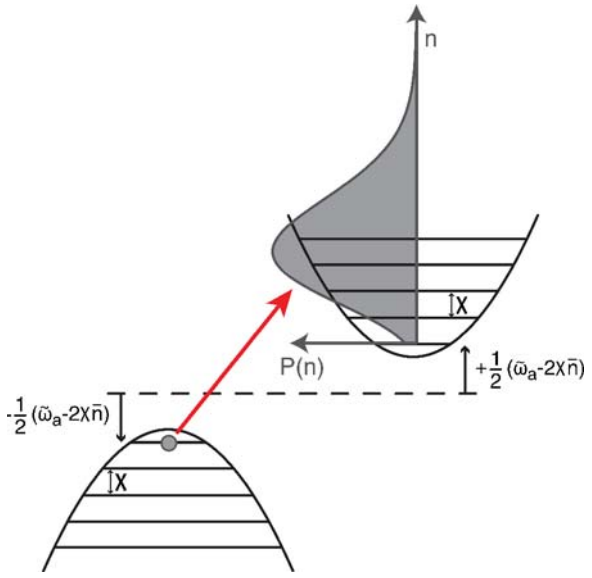


FIG. 10. (Color online) Pictorial representation of the dispersive Hamiltonian in a frame defined by Eq. (5.33) at $\Delta_r=0$. When calculating the correlator $\langle\hat{\sigma}_-(t)\hat{\sigma}_+(0)\rangle$, the qubit is flipped at time $t=0$. In the displaced frame, this corresponds to both flipping the qubit and displacing the oscillator from the vacuum state to a coherent state with mean photon number $4\bar{n}$. This distribution is shown on top of the harmonic oscillator corresponding to the qubit in its excited state. This simple picture explains the observed peaks in the qubit power spectrum and the presence of negative shifts.

$$\hat{D}[\alpha] = \exp(\alpha\hat{a}^\dagger - \alpha^*\hat{a}), \tag{5.34}$$

and $\hat{\Pi}_\pm$ are the projectors for the excited and ground state of the qubit. That is, we move to a frame that takes both the pointer states out of the picture. In this frame, Eq. (2.5) becomes

$$\hat{H} = \frac{\hbar}{2}(\tilde{\omega}_a - 2\chi\bar{n})\hat{\sigma}_z + \hbar\chi\hat{a}^\dagger\hat{a}\hat{\sigma}_z. \tag{5.35}$$

Here we have considered the situation where $\Delta_r=0$ and neglected the last term of Eq. (2.5) which only leads to a small shift of the qubit transition frequency in the present situation. This Hamiltonian is pictorially represented in Fig. 10. We immediately see that, in this frame, the qubit transition frequency is reduced by $2\chi\bar{n}$ from the Lamb-shifted frequency $\tilde{\omega}_a$. Moreover, when the qubit is in the ground state, the Hamiltonian corresponds to a shifted and inverted harmonic oscillator [left-hand side (LHS) of Fig. 10]. On the other hand, when the qubit is in the excited state, the harmonic oscillator is shifted but not inverted [right-hand side (RHS) of Fig. 10]. Starting with the qubit initially in the ground state and the field in a coherent state of amplitude $\alpha_-$ corresponds, in the frame defined by Eq. (5.33), to a qubit in the ground state and the vacuum state of the oscillator. In this frame, flipping the qubit at time $t=0$ corresponds to applying the operator (for $\Delta_r=0$)

$$\hat{U}^\dagger\hat{\sigma}_+\hat{U} \propto \hat{\sigma}_+\hat{D}[\alpha_- - \alpha_+] = \hat{\sigma}_+\hat{D}[2\sqrt{\bar{n}}]. \tag{5.36}$$

The result is both to flip the qubit and to displace the oscillator to a coherent state of mean photon number $4\bar{n}$. This is exactly the observed structure in the qubit power spectrum and each of the observed peaks corresponds to one of the possible transitions between these two oscillators. We note that the above is similar to the Mollow triplet, where transitions both above and below the atomic transition frequency are possible due to dressing of the atomic levels by the presence of a strong pump drive [39].

Observation of number splitting would constitute a simple test of number quantization of the field inside the resonator in the dispersive regime. In the resonant regime ($\Delta=\Delta_r=0$), number quantization has been verified in cavity QED using Rydberg atoms [21]. This was done by looking at the Fourier components in the probability of finding the atom in the excited state as a function of time. In the dispersive regime ($\Delta > g, \kappa$) the recurrence time for the cavity field was too long to be observable [22]. In the circuit QED system it should be possible to reach the strong-dispersive limit $\chi > \kappa, 1/T_2$ where it is possible to probe number quantization. In the dispersive regime the qubit spectrum acts as a probe of the cavity field. When the rate at which information about the cavity state is passed to the qubit faster than the rate at which the cavity state changes significantly due to damping and qubit dephasing, it is possible to learn about the statistics of the field from the qubit spectrum. Note the above predictions are valid only in the limit where $\chi^2/\Delta < \kappa$. When this is not the case the higher-order effects in the Jaynes-Cummings Hamiltonian [Eq. (2.3)] will become important and will lead to non-Poissonian statistics of the resonator field. This will be discussed further elsewhere. Finally, we note an interesting proposal by Brune *et al.* [29,30] and a recent experiment [32] to prepare a Fock state of the cavity field (number squeezing) containing a single photon by monitoring the state of a continuous beam of atoms sent through the cavity.

## VI. CONCLUSION

We have found that, due to the ac Stark shift, quantum noise in the photon number populating the resonator leads to well-characterized measurement-induced dephasing. A simple model based on a Gaussian approximation for the phase noise was presented, as well as a more general model based on the positive-$P$ function. For the experimental parameters given in the Letter, both models yield the same quantitative results which are in very good agreement with the experiment. We emphasize that the only adjustable parameter in the theory is the intrinsic qubit dephasing rate whose only effect is to give a constant offset to the predicted linewidth.

In the strong dispersive regime, where the cavity pull $\chi$ is much bigger than the cavity field decay rate $\kappa/2$, the $P$-function approach predicts a splitting of the qubit spectrum due to the discrete quantum nature of the field populating the cavity. Observation of this prediction would be a confirmation of the quantized nature of the resonator field. This strong-dispersive-coupling regime should be readily achievable with realistic circuit QED parameters.

## ACKNOWLEDGMENTS

We are grateful to Howard Wiseman for discussions. This work was supported in part by the National Security Agency (NSA) under Army Research Office (ARO) Contract No. DAAD19-02-1-0045, the NSF under Grant Nos. ITR-0325580 and DMR-0342157, and the W. M. Keck Foundation. A.B. was partially supported by the Natural Sciences and Engineering Research Council of Canada (NSERC), the Canadian Institute for Advanced Research (CIAR), and D-Wave Systems Inc.


## APPENDIX A: POSITIVE-*P* REPRESENTATION

In this appendix, we show how to solve the master equation Eq. (2.6) in the presence of a measurement drive but take the spectroscopy drive $\varepsilon_s=0$. Substituting Eq. (5.13) into Eq. (2.6) yields the following four coupled differential equations:

$$\dot{\hat{\rho}}_{ee} = \kappa\mathcal{D}[\hat{a}]\hat{\rho}_{ee} - \gamma_1\hat{\rho}_{ee} - i\varepsilon_{\rm rf}[\hat{a}+\hat{a}^\dagger,\hat{\rho}_{ee}] - i\chi[\hat{a}^\dagger\hat{a},\hat{\rho}_{ee}] - i\Delta_r[\hat{a}^\dagger\hat{a},\hat{\rho}_{ee}], \tag{A1}$$

$$\dot{\hat{\rho}}_{gg} = \kappa\mathcal{D}[\hat{a}]\hat{\rho}_{gg} + \gamma_1\hat{\rho}_{ee} - i\varepsilon_{\rm rf}[\hat{a}+\hat{a}^\dagger,\hat{\rho}_{gg}] + i\chi[\hat{a}^\dagger\hat{a},\hat{\rho}_{gg}] - i\Delta_r[\hat{a}^\dagger\hat{a},\hat{\rho}_{gg}], \tag{A2}$$

$$\dot{\hat{\rho}}_{eg} = \kappa\mathcal{D}[\hat{a}]\hat{\rho}_{eg} - \gamma_2\hat{\rho}_{eg} - i\varepsilon_{\rm rf}[\hat{a}+\hat{a}^\dagger,\hat{\rho}_{eg}] - i\chi\{\hat{a}^\dagger\hat{a},\hat{\rho}_{eg}\} - i\Delta_r[\hat{a}^\dagger\hat{a},\hat{\rho}_{eg}] - i\tilde{\omega}_a\hat{\rho}_{eg}, \tag{A3}$$

$$\dot{\hat{\rho}}_{ge} = \kappa\mathcal{D}[\hat{a}]\hat{\rho}_{ge} - \gamma_2\hat{\rho}_{ge} - i\varepsilon_{\rm rf}[\hat{a}+\hat{a}^\dagger,\hat{\rho}_{ge}] + i\chi\{\hat{a}^\dagger\hat{a},\hat{\rho}_{ge}\} - i\Delta_r[\hat{a}^\dagger\hat{a},\hat{\rho}_{ge}] + i\tilde{\omega}_a\hat{\rho}_{ge}. \tag{A4}$$

Solving these four differential equations would yield a complete solution. However, because of the coupling introduced by $\gamma_1$, this is not possible analytically for all possible observables. However, for the particular case of computing the dephasing rate, we can (without error) set $\gamma_1=0$ in the equations for $\hat{\rho}_{ee}$ and $\hat{\rho}_{gg}$ while keeping the contribution of relaxation to dephasing in the equations for the off-diagonal components.

To solve Eqs. (A1)–(A4) we express the density matrix under the positive-*P* representation [31]:

$$\hat{\rho}_{ij} = \int d^2\alpha \int d^2\beta \frac{|\alpha\rangle\langle\beta^*|}{\langle\beta^*|\alpha\rangle} P_{ij}(\alpha,\beta). \tag{A5}$$

Using this expression in Eqs. (A1)–(A4) and the identities

$$\hat{a}|\alpha\rangle = \alpha|\alpha\rangle, \tag{A6}$$

$$\hat{a}^\dagger|\alpha\rangle = (\partial_\alpha + \alpha^*/2)|\alpha\rangle, \tag{A7}$$

$$\langle\beta^*|\hat{a}^\dagger = \beta\langle\beta^*|, \tag{A8}$$

$$\langle\beta^*|\hat{a} = (\partial_\beta + \beta/2)\langle\beta^*|, \tag{A9}$$

gives four coupled differential equations for the "probability densities" $P_{ij}$:

$$\dot{P}_{ee} = \partial_\alpha[(i\varepsilon_{\rm rf} + i\chi\alpha + i\Delta_r\alpha + \kappa\alpha/2)P_{ee}] + \partial_\beta[(-i\varepsilon_{\rm rf} - i\chi\beta - i\Delta_r\beta + \kappa\beta/2)P_{ee}], \tag{A10}$$

$$\dot{P}_{gg} = \partial_\alpha[(i\varepsilon_{\rm rf} - i\chi\alpha + i\Delta_r\alpha + \kappa\alpha/2)P_{gg}] + \partial_\beta[(-i\varepsilon_{\rm rf} + i\chi\beta - i\Delta_r\beta + \kappa\beta/2)P_{gg}], \tag{A11}$$

$$\dot{P}_{eg} = \partial_\alpha[(i\varepsilon_{\rm rf} + i\chi\alpha + i\Delta_r\alpha + \kappa\alpha/2)P_{eg}] + \partial_\beta[(-i\varepsilon_{\rm rf} + i\chi\beta - i\Delta_r\beta + \kappa\beta/2)P_{eg}] - i2\chi\alpha\beta P_{eg} - \gamma_2 P_{eg} - i\tilde{\omega}_a P_{eg}, \tag{A12}$$

$$\dot{P}_{ge} = \partial_\alpha[(i\varepsilon_{\rm rf} - i\chi\alpha + i\Delta_r\alpha + \kappa\alpha/2)P_{ge}] + \partial_\beta[(-i\varepsilon_{\rm rf} - i\chi\beta - i\Delta_r\beta + \kappa\beta/2)P_{ge}] + i2\chi\alpha\beta P_{ge} - \gamma_2 P_{ge} + i\tilde{\omega}_a P_{ge}. \tag{A13}$$

To obtain these expressions, we have assumed that $P_{ij}(\infty,\infty)=0$ as is usual [25].

These equations can be solved simply by making the *Ansatze*

$$P_{ee} = \delta^{(2)}[\alpha-\alpha_+(t)]\delta^{(2)}[\beta-\alpha_+^*(t)],$$

$$P_{gg} = \delta^{(2)}[\alpha-\alpha_-(t)]\delta^{(2)}[\beta-\alpha_-^*(t)],$$

$$P_{eg} = a_{eg}(t)\,\delta^{(2)}[\alpha-\alpha_+(t)]\delta^{(2)}[\beta-\alpha_-^*(t)],$$

$$P_{ge} = a_{ge}(t)\,\delta^{(2)}[\alpha-\alpha_-(t)]\delta^{(2)}[\beta-\alpha_+^*(t)] \tag{A14}$$

and substitute these into each equation. This results in

$$\dot{\alpha}_+ = -i\varepsilon_{\rm rf} - i(\Delta_r + \chi - i\kappa/2)\alpha_+, \tag{A15}$$

$$\dot{\alpha}_- = -i\varepsilon_{\rm rf} - i(\Delta_r - \chi - i\kappa/2)\alpha_-, \tag{A16}$$

$$\dot{a}_{eg} = -i(\tilde{\omega}_a - i\gamma_2)a_{eg} - i2\chi\alpha_+\alpha_-^* a_{eg}, \tag{A17}$$

$$\dot{a}_{ge} = i(\tilde{\omega}_a + i\gamma_2)a_{ge} + i2\chi\alpha_-\alpha_+^* a_{ge}. \tag{A18}$$

Solving these simple differential equations completely solves the master equation Eq. (2.6) in the absence of mixing due to $T_1$ effects. The solution is given in Eqs. (5.14)–(5.18).

## APPENDIX B: MEASUREMENT TIME

In this appendix we show how one can calculate the measurement time for this system and show how it relates to the quantum limit [35]. To do this we need to describe how we are measuring the pointer states (i.e., how the information is processed). In this experiment, this is done by using heterodyne detection of the signal that is transmitted from the cavity. In other words, the full quantum trajectory for the system is [40,41]

$$d\rho_J(t) = dt\,\mathcal{L}\rho_J(t) + dt\,\mathcal{H}\{[J^*(t) - \kappa\eta\langle\hat{a}^\dagger\rangle]\hat{a}\}\rho_J(t), \tag{B1}$$

where $\mathcal{H}\{[J^*(t)-\kappa\eta\langle\hat{a}^\dagger\rangle]\hat{a}\}\rho_J(t)$ is the superoperator representing the nonlinear effects of the continuous monitoring and is defined by

$$\mathcal{H}[\hat{A}]\rho = \hat{A}\rho + \rho\hat{A}^{\dagger} - \langle \hat{A} + \hat{A}^{\dagger}\rangle\rho. \tag{B2}$$

The measurement record (heterodyne signal) is given by

$$J(t) = \kappa\eta\langle\hat{a}\rangle + \sqrt{\kappa\eta}\zeta(t), \tag{B3}$$

where $\zeta(t)$ is a complex Gaussian white noise term, which is formally defined as

$$E[\zeta(t)\zeta(t')] = E[\zeta(t)] = 0, \tag{B4}$$

$$E[\zeta(t)\zeta^{*}(t')] = \delta(t-t'), \tag{B5}$$

where $E$ denotes an ensemble average and $\eta = 1/[2(N+1)]$ is the inefficiency of the measurement. Here $N$ is the dark noise and the extra factor of $1/2$ is due to the fact that information leaks out of the cavity in both directions and we only monitor transmission [13].

From this quantum trajectory the rate at which information is obtained about $\langle\hat{a}\rangle$ is $\kappa\eta$. To convert this to a rate of information gain about $\langle\hat{\sigma}_z\rangle$ we define the measurement observable for a time $\tau$ as

$$I(\tau) = \frac{1}{\tau}\int_0^{\tau} \mathrm{Re}[J(t)e^{-i\phi}]dt, \tag{B6}$$

where $\phi$ determines the quadrature in which the information about the qubit is encoded. This can be determined by

$$\tan\phi = \frac{\mathrm{Im}(\alpha_+^s - \alpha_-^s)}{\mathrm{Re}(\alpha_+^s - \alpha_-^s)}. \tag{B7}$$

For example, if $\Delta_r = 0$ and $\phi = 0$, the information about the qubit is encoded only into the real part of $\langle\hat{a}\rangle$. From this observable, the mean and variance are

$$\bar{I}(\tau) = \kappa\eta\,\mathrm{Re}(\langle\hat{a}\rangle e^{-i\phi}), \tag{B8}$$

$$\Delta|I(\tau)| = \sqrt{\langle[I(\tau) - \bar{I}(\tau)]^2\rangle} = \sqrt{\frac{\kappa\eta}{2\tau}}. \tag{B9}$$

That is, if we were to measure the system for a time $\tau$ many times we are confident that to one standard deviation the value of $\bar{I}$ is $\kappa\eta\mathrm{Re}(\langle\hat{a}\rangle e^{-i\phi}) \pm \sqrt{\kappa\eta/2\tau}$.

If $\tau$ is much shorter than $1/\gamma$ then we can approximate $\bar{I}(\tau)$ with $\bar{I}_{\pm}(\tau) = \kappa\eta\mathrm{Re}(\alpha_{\pm}^s e^{-i\phi})$, where the $\pm$ subscript refers to the state of the qubit. To be able to distinguish between $\langle\hat{\sigma}_z\rangle = \pm 1$, we require $\Delta\langle\hat{\sigma}_z\rangle \leqslant 1$ and thus

$$\Delta|I| \leqslant \frac{|\bar{I}_+ - \bar{I}_-|}{2} = \frac{\kappa\eta\sqrt{D_s}}{2}. \tag{B10}$$

The equality defines the measurement time $t_{\mathrm{meas}}$. Using the above, this can be rewritten as

$$t_{\mathrm{meas}}\Gamma_{\mathrm{m}} = \frac{1}{\eta}. \tag{B11}$$

That is, even for perfect detection efficiency $\eta = 1$, this approach is a factor of 2 away from the quantum limit $t_{\mathrm{meas}}\Gamma_{\mathrm{m}} = 1/2$ [35]. This is because even though we are selecting the correct quadrature in which the information about the qubit is stored [using the classical processing defined in Eq. (B7)], we are still measuring the other quadrature as we are performing heterodyne detection. It is well known that heterodyne detection measures both the $\phi$ and $\phi + \pi/2$ quadrature with $1/2$ efficiency [42,43]. Thus if we change the detection scheme to homodyne detection of the $\phi$ quadrature we can reach the quantum limit. That is, to reach the quantum limit we require $\eta = 1$ which means we need asymmetric cavities and no dark noise as well as a detection scheme that extracts only information about $\hat{\sigma}_z$. Note that if we did not perform any classical processing on the heterodyne signal $J(t)$ then we would be a factor of 4 away from the quantum limit.


[1] M. H. Devoret, A. Wallraff, and J. M. Martinis, e-print cond-mat/0411174.

[2] A. Wallraff, D. I. Schuster, A. Blais, L. Frunzio, J. Majer, M. H. Devoret, S. M. Girvin, and R. J. Schoelkopf, Phys. Rev. Lett. **95**, 060501 (2005).

[3] I. Chiorescu, Y. Nakamura, C. Harmans, and J. Mooij, Science **299**, 1869 (2003).

[4] D. Vion, A. Aassime, A. Cottet, P. Joyez, H. Pothier, C. Urbina, D. Esteve, and M. Devoret, Science **296**, 886 (2002).

[5] J. M. Martinis, S. Nam, J. Aumentado, and C. Urbina, Phys. Rev. Lett. **89**, 117901 (2002).

[6] Y. Nakamura, Y. Pashkin, and J. Tsai, Nature (London) **398**, 786 (1999).

[7] R. McDermott, R. W. Simmonds, M. Steffen, K. B. Cooper, K. Cicak, K. D. Osborn, S. Oh, D. P. Pappas, and J. M. Martinis, Science **307**, 1299 (2005).

[8] J. B. Majer, F. G. Paauw, A. C. J. ters Haar, C. J. P. M. Harmans, and J. E. Mooij, Phys. Rev. Lett. **94**, 090501 (2005).

[9] T. Yamamoto, Y. A. Pashkin, O. Astafiev, Y. Nakamura, and J. Tsai, Nature (London) **425**, 941 (2003).

[10] A. J. Berkley, H. Xu, R. C. Ramos, M. A. Gubrud, F. W. Strauch, P. R. Johnson, J. R. Anderson, A. J. Dragt, C. J. Lobb, and F. C. Wellstood, Science **300**, 1548 (2003).

[11] Y. A. Pashkin, T. Yamamoto, O. Astafiev, Y. Nakamura, D. Averin, and J. Tsai, Nature (London) **421**, 823 (2003).

[12] Y. Makhlin, G. Schön, and A. Shnirman, Rev. Mod. Phys. **73**, 357 (2001).

[13] A. Blais, R.-S. Huang, A. Wallraff, S. M. Girvin, and R. J. Schoelkopf, Phys. Rev. A **69**, 062320 (2004).

[14] A. Blais, A. Maassen van den Brink, and A. H. Zagoskin, Phys. Rev. Lett. **90**, 127901 (2003).

[15] F. Plastina and G. Falci, Phys. Rev. B **67**, 224514 (2003).

[16] J. Q. You and F. Nori, Phys. Rev. B **68**, 064509 (2003).

[17] A. Wallraff, D. I. Schuster, A. Blais, L. Frunzio, R.-S. Huang,

J. Majer, S. Kumar, S. M. Girvin1, and R. J. Schoelkopf, Nature (London) **431**, 162 (2004).
[18] I. Chiorescu, P. Bertet, K. Semba, Y. Nakamura, C. J. P. M. Harmans, and J. E. Mooij, Nature (London) **431**, 159 (2004).
[19] D. I. Schuster, A. Wallraff, A. Blais, L. Frunzio, R.-S. Huang, J. Majer, S. M. Girvin, and R. J. Schoelkopf, Phys. Rev. Lett. **94**, 123602 (2005).
[20] H. Xu *et al.*, Phys. Rev. Lett. **94**, 027003 (2005).
[21] M. Brune, F. Schmidt-Kaler, A. Maali, J. Dreyer, E. Hagley, J. M. Raimond, and S. Haroche, Phys. Rev. Lett. **76**, 1800 (1996).
[22] M. Brune, E. Hagley, J. Dreyer, X. Maitre, A. Maali, C. Wunderlich, J. M. Raimond, and S. Haroche, Phys. Rev. Lett. **77**, 4887 (1996).
[23] J. M. Raimond, M. Brune, and S. Haroche, Phys. Rev. Lett. **79**, 1964 (1997).
[24] T. Meunier, S. Gleyzes, P. Maioli, A. Auffeves, G. Nogues, M. Brune, J. M. Raimond, and S. Haroche, Phys. Rev. Lett. **94**, 010401 (2005).
[25] C. Gardiner and P. Zoller, *Quantum Noise* (Springer-Verlarg, Berlin, 2000).
[26] V. Bouchiat, D. Vion, P. Joyez, D. Esteve, and M. Devoret, Phys. Scr., T **76**, 165 (1998).
[27] L. Frunzio, A. Wallraff, D. I. Schuster, J. Majer, and R. J. Schoelkopf, IEEE Trans. Appl. Supercond. **15**, 860 (2004).
[28] J. Raimond, M. Brune, and S. Haroche, Rev. Mod. Phys. **73**, 565 (2001).
[29] M. Brune, S. Haroche, V. Lefevre, J. M. Raimond, and N. Zagury, Phys. Rev. Lett. **65**, 976 (1990).
[30] M. Brune, S. Haroche, J. M. Raimond, L. Davidovich, and N. Zagury, Phys. Rev. A **45**, 5193 (1992).
[31] D. Walls and G. Milburn, *Quantum Optics* (Spinger-Verlag, Berlin, 1994).
[32] G. Nogues, A. Rauschenbeutel, S. Osnaghi, M. Brune, J. M. Raimond, and S. Haroche, Nature (London) **400**, 239 (1999).
[33] A. Abragam, *The Principles of Nuclear Magnetism* (Oxford University Press, Oxford, 1961).
[34] C. Gardiner, *Handbook of Stochastic Methods: for Physics, Chemistry and the Natural Science* (Springer-Verlag, Berlin, 1985).
[35] A. A. Clerk, S. M. Girvin, and A. D. Stone, Phys. Rev. B **67**, 165324 (2003). We note that in this paper, the definition of the quantum limit differs by a factor of 2 from what has been used here. This is because these authors used a different definition for the measurement time.
[36] G. J. Milburn and H. M. Wiseman (unpublished).
[37] A. Blais *et al.* (unpublished).
[38] M. I. Dykman and M. A. Krivoglaz, Sov. Phys. Solid State **29**, 211 (1987).
[39] B. Mollow, Phys. Rev. A **5**, 1522 (1971).
[40] H. M. Wiseman and G. J. Milburn, Phys. Rev. A **47**, 1652 (1993).
[41] H. M. Wiseman and L. Diósi, Chem. Phys. **268**, 91 (2001).
[42] H. A. Haus and C. H. Townes, Proc. IRE **50**, 1544 (1962).
[43] H. P. Yuen and J. H. Shapiro, IEEE Trans. Inf. Theory **26**, 78 (1980).